Mechanical and fracture properties of concrete reinforced with recycled and industrial steel fibers using Digital Image Correlation technique and X-ray micro computed tomography

Łukasz Skarżyński *, Jan Suchorzewski

Faculty of Civil and Environmental Engineering, Gdańsk University of Technology, Poland

HIGHLIGHTS

- Steel fibers from end-of-life tyres (ELT) are promising application as a concrete dispersed reinforcement.
- We compare mechanical properties of plain concrete and concrete reinforced with recycled and industrial fibers.
- We show fracture process zone development using Digital Image Correlation during wedge splitting test (WST).
- We present 3D images from X-ray micro-CT of material micro-structure, distribution of air voids and fibers.
- We analyse shape, width and curvature of crack during deformation process using X-ray micro-CT in 3D.

ABSTRACT

Paper presents investigation of fracture phenomenon in plain concrete and in concrete reinforced with both recycled steel fibers (RSF) and industrial steel fibers (ISF). The wedge splitting test (WST), which enables stable crack propagation for quasi-brittle materials, was carried out on $75 \times 75 \times 75$ mm cube samples. Initially, fracture process zone development was investigated only on the surface of samples using Digital Image Correlation which is a non-destructive optical testing method. Furthermore, to analyse the 3D cracking phenomenon (formation, development, width, shape and curvature) X-ray micro computed tomography was used. Micro-CT images were taken during continuous deformation process - without unloading sample during scanning. X-ray micro-computed tomography was also used to visualise and characterise air voids and fibers (length, diameter and orientation) embedded in concrete. The mechanical properties of plain, RSF and ISF reinforced concrete in terms of compressive strength, tensile splitting strength, shrinkage, tensile and residual strength in 3-point bending were additionally described.

© 2018 Elsevier Ltd. All rights reserved.

1. Introduction

Fracture process is a fundamental phenomenon in quasi-brittle materials like concrete [1–3]. It is very complex since it consists of main cracks with various branches, secondary cracks and micro-cracks [1]. During fracture, micro-cracks first arise in a hardening region on the stress-strain curve which change gradually during material softening into dominant distinct macroscopic cracks up to failure. The fracture process strongly depends upon a heterogeneous structure of materials over many different length scales, changing e.g. in concrete from the few nanometres (hydrated cement) to the millimetres (aggregate particles). Thus, understanding of a fracture process is of major importance to ensure the safety of the structure and to optimize the material behaviour.

Concrete is widely regarded as a brittle material due to its low tensile, and high compression strength. Nowadays, in order to increase ductility and material strength, most popularly industrial steel fibers (ISF) are added to concrete matrix. ISF can be of different types (hooked ended, corrugated etc.), lengths and diameters with the recommended content between 1.5% and 3% [4]. Studies of steel-fiber reinforced concrete are mainly focused on the effects of the geometric types, volume fraction and strength of steel fibers on the flexural or compressive behavior [4–7]. The use of steel fibers in concrete was expanded to the application of various fibers, such as synthetic, glass and carbon fibers or organic fibers. In particular steel and synthetic fibers were used to assess the properties and performance of concrete [8–10]. The influence of the combination

of steel and synthetic fibers in the flexural strength and ductility of concrete was also analysed with respect to the shape, length and dosage of the fibers. In addition, several researchers examined the influence of the steel fibers in combination with steel bars reinforced concrete (hybrid reinforcement) [11].

Our interests concern ground floor slabs that are integral to the efficient operation of an industrial facility. Industrial floors are normally subjected to various types of loading and have common requirements of high strength, toughness, crack control and durability among others. The use of industrial steel fibers (ISF) in concrete flooring is advantageous over conventional grade slab wherein the residual load-carrying capacity is used and thus, increases the strength, toughness and results in economy of floor thickness apart from saving in construction time. Recently steel fibers recovered (RSF) from end-of-life tyres have been in the center of attention of researchers. Tyres are 100% recyclable and all components, i.e. rubber, metals and textiles, can be recycled and re-used in many commercial products, as concrete. Nowadays, there is a growing trend to use industrial wastes or by-products in the production of cementitious composite. A significant number of experimental studies have been conducted regarding the use of metal waste recycled fibers as a reinforcement and other industrial waste as admixtures or aggregate grains (recycled aggregate, PET or polyurethane foam light-weight aggregate) in the production of cementitious composite. The use of wastes in system of concrete elements has beneficial environmental and economic impacts. Strengthening concrete matrix with inhomogeneous recycled fibers (RSF), made of high quality steel, improves concrete mechanical properties such as: shrinkage, compressive strength, tensile strength, residual strength [12–16].

Except for mentioned mechanical properties, to preserve safety and durability of the fiber reinforced industrial floors a fracture phenomenon i.e. crack formation, evolution, shape and width should be carefully investigated. However, a direct observation of fracture is difficult because of a small scale at which microstructural events interact with a failure process. Different techniques like scanning electron microscopy (SEM) [17–19], high speed photography [20], laser speckle interferometry [21,22], acoustic emission [23–27], X-ray technique [28–31], Moiré method [32,33] and Digital Image Correlation (DIC) technique [34–39] have been used to experimentally investigate a fracture process in quasi-brittle materials (concrete, rock and masonry) at the laboratory scale.

The paper gives an insight into the possibilities of recycled steel fibres (RSF) to be used as an industrial floor reinforcement. The mechanical properties of plain, RSF and ISF reinforced concrete in terms of compressive strength, tensile splitting strength, shrinkage, tensile and residual strength in 3-point bending were described. However, the main objective and novelty of this study is to investigate fracture phenomenon in plain concrete and concrete reinforced both with ISF and RSF during wedge splitting test. Initially, fracture process zone development was investigated only on the surface of samples using Digital Image Correlation (DIC). Afterwards, to analyze 3D cracking phenomenon (formation, width, shape and curvature) X-ray micro computed tomography (micro-CT) images were taken during continuous deformation process (without unloading during scanning). This technique allows to obtain a continuous CMOD-force curve and preserve crack from closing during scanning. Moreover, X-ray micro-CT was used to visualize, measure and characterize fibers embedded in concrete.

2. DIC and micro-CT technique

The DIC technique has become one of the most popular method of fracture examination due to its availability, simplicity and low cost. In DIC method material displacements are obtained by tracking a random speckle pattern applied to the surface by means of digital images at different instances of deformation. Next strains, which are the best indicator for fracture process zones, based on displacements are calculated using standard finite-element shape functions. The method gives high resolution measurements of a displacement field. A correct local displacement vector for each interrogation cell is accomplished by means of a cross-correlation function between two consecutive brightness distributions in two digital images. The function calculates simply possible displacements by correlating all gray values from the first image with all gray values from the second image. The correlation plane is evaluated at single pixel intervals, what means that the resolution is equal to one pixel. By fitting an interpolation function to the region close to the peak, the displacement vector is established with a high accuracy (equal to the correlation offset). The peak in the correlation function indicates that two images are overlaying each other (thus, it indicates the 'degree of match' between two images). We used the Pearson's product-moment correlation function. The peak (best match) of the correlation function is usually not clearly distinguished as the correlation function produces results for each pixel of image. To precisely locate the peak, a sub-pixel interpolation was performed. As an interpolation function, the function sinc256 was used. It has been shown that the accuracy in strain measurements when compared with strain gauge data is within ±200μ. The performance of DIC is affected by many factors such as interpolation algorithm, shape function, subset size, sub pixel registration algorithm, sensor noise and lens distortion. DIC can be used both for 2D and 3D measurements. While 2D deformations can be measured with one camera, 3D deformations require use of two cameras both measuring the changes of the deformed surface at different angle. DIC technique allows to identify local strain mapping that can be used in determination of the fracture process zones and cracks that are certainly two key parameters needed to estimate the permeability, strength and durability of structural concrete components [34–39], Moreover, full-field DIC experiments allow to determine Young modulus, Poisson ratio and measure off-plane properties [40]. DIC is widely used optical method for shape motion [41] and evaluation of creep degradation [42]. DIC technique can be applied to measurements of different materials like wood, concrete, polymers, steel etc. DIC is also widely used in experimental measurements of concrete reinforced with fibers [43–45]. However, this method has two drawbacks: (1) no information about microstructure and (2) no fracture process zone / crack (its shape and width) inside material can be achieved.

Recently, the application of high-resolution X-ray micro computed tomography significantly increased. The basic idea of this imaging technique goes back to Johan Radon, who proved in 1917 that an n-dimensional object can be reconstructed from its (n-1)-dimensional projections. However, the mathematical basis for the actual CT image reconstruction was presented by Cormack in 1964 and 1965. About 10 years later, Hounsfield submitted a patent, describing the first CT scanner, which was then built in 1975. The possibility of non-invasively imaging three-dimensional sections of a human body was of such importance that Cormack and Hounsfield were awarded with the Nobel Price for Medicine in 1979. Micro-CT is a non-destructive technique that provides three-dimensional images of the objects internal structure. The basic physical X-ray principal of computed tomography is the interaction of ionizing radiation with material, where the so-called photo-effect builds the main interaction mechanism. The photo-effect attenuates the photons proportionally to the third power of the order number of the elements and inverse proportional to the third power of the photon energy. Thus, the actual attenuation not only depends on the material but also on the

energy spectrum of the X-ray source. As an X-ray beam penetrates an object, it is exponentially attenuated according to the material along its path. The energy-dependent material constant appearing in the exponent of this attenuation formula is called the linear attenuation coefficient. It expresses the amount of radiation that is attenuated on an infinitely small distance, in which the final attenuation reflects the sum of all these local linear attenuations along the X-ray beam. Therefore, an X-ray projection (or X-ray image) represents an image of the sum of all local attenuations along the X-ray beam. The 3D images of the interior of an object are obtained by collecting a series of 2D images that are stored while the sample is rotated. With the development of micro-CT, complementary techniques as well as new image processing algorithms and analysis techniques have evolved. These new techniques opened the field of micro-CT to many new applications. Imaging techniques with image analysis offer the possibility to analyse the size and shape of each individual particle present in a sample. Especially X-ray micro computed tomography provides a powerful tool for non-destructive analysis in 3D. Various image analysis methods are used to obtain quantitative information about the size and shape of particles. For each particle a variety of different specific measurements can be performed (e.g. location, size and shape). In these methods touching particles are separated, so that each individual particle can be identified, counted and measured. The powerful imaging capabilities of X-ray tomography are now available in a range instruments suitable for microscopic imaging of small objects with a wide range of applications such as 3D biomedical [46,47], food studies [48], soft tissue research [49,50], insects and fishes, microelectronics, materials [29,30,51–55], geological studies [56,57], cementitious materials and more. X-ray micro computed tomography has been recently often used as a powerful tool for analysis of fiber reinforced concrete. Fibers orientation and distribution as well as air voids were analysed in Refs. [58–64]. However, there is still lack of information about 3D evolution of shape, width and curvature of fracture during the continuous deformation process for plain concrete and for concrete reinforced with ISF and RSF.

3. Mix design and fiber characterisation

The concrete was prepared from Portland cement (CEM II/B-S 42.5N-NA), aggregate and water. Three fractions of aggregate were used: sand with the aggregate grain size between 0 and 2 mm, gravel with the aggregate grain size between 2 and 8 mm and gravel with the aggregate grain size between 8 and 16 mm. The sand point was equal to 43% and the water to cement ratio was equal to 0.50. A small superplasticizer quantity was used to improve the workability of the fresh concrete mix. When adding steel fibers, the concrete mix was modified - the volume of aggregate was replaced by the volume of added fibers. In our experiments 25 kg/m^3 (0.25% in volume) of industrial BAUMIX fibers WLS-25/0.5/H (diameter d_{If} = 0.5 mm and length l_{If} = 25 mm) with the hooked ends and 50 kg/m^3 (0.50% in volume) of recycled steel fibers were added. The final amount of ISF was chosen as the most typically used in every day engineering practice at the building site for industrial floors in Poland. Theoretically the minimum amount of fibers should be greater, however due to economic issues contractors in Poland most commonly use 25 kg/m^3 of fibers. The final mixture using 50 kg/m^3 of RSF was chosen to obtain similar tensile strength in wedge splitting test as for concrete reinforced with 25 kg/m^3 of ISF. Our main objective was to compare fracture process in reinforced concrete of similar strength. As the recycled fibers have very differentiated lengths, diameters and aspect ratio (fibers were not initially sorted in terms of diameter and length) some of them are passive in fracture process [65]. That is why more RSF

have to be used comparing to ISF. The detailed report form preliminary tests concerning determination of the RSF fiber quantity will be published soon in PhD of Magda Pawelska-Mazur (see Acknowledgements). The used mix proportions are depicted in Table 1.

Recycled fibers were obtained in the shredding tyres at ambient temperature. This is the most commonly used method of mechanical tyre shredding. Pre-cut tyres are ground with special mills i.e. granulators or rolling mills. In order to remove the fibers from the textile cord, pneumatic separation is used and the steel fibers are removed by means of an electromagnet. In the mechanical grinding process, rubber particles of various sizes are obtained: rubber dust and granulate. The resulting fine or granulated rubber has an irregular shape and an unfolded frayed surface. In addition to rubber, steel and textile waste are also obtained. It should be emphasized that this process is very energy-intensive (about 125 kWh/1 ton of tyres) and that it is accompanied by a large noise emission.

Recycled fibers diameter and length can be attributed to the different origins of the waste tyres from which the recycled fibers are derived (i.e. exhausted waste tyres from different kinds of vehicles: cars, trucks etc.). Caggiano et al. [13] manually measured 2000 fibers and performed their detailed geometric characterization. The fiber diameter d_{Rf} ranged between 0.11 and 0.44 mm. An average value of 0.25 mm and a median value of around 0.22 mm with a standard deviation of 0.07 mm were evaluated. The recycled fiber length l_{Rf} ranged between 6 and 74 mm. An average value of 26.17 mm, a modal value of 20.00 mm (with a range 18–21 mm) and a median value of around 25.00 mm with a standard deviation of 9.52 mm were evaluated. The Curvature Index (CI) representing a shape index aimed at evaluation the curvature of the fiber (if CI is equal to 0% the fiber is completely stretched, otherwise, if CI is equal to 100%, fiber is fully curved) was lower than 20% in almost 60% of the sampled fibers which means that fibers used in study were quite aligned with limited curls and/or twists. Aspect ratio (λ) defined as the ratio between the fiber length (l_{Rf}) and its diameter (d_{Rf}), was highly variable between 17.48 and 321.74 with average value of 109.5, modal value of 100, median value around 101 and standard deviation of 45.55.

In our experiments, diameter and length of the fibers embedded in concrete were evaluated using X-ray micro computed tomography. High energy, extended table scanner SkyScan 1173 with the 130 keV microfocus X-ray source, flat panel sensor of large format (5 Mpx) with special protection by a lead-glass fiber-optic window for achieving a long lifetime under high energy X-ray was used. Scanner is additionally equipped with precision object manipulator with and integrated micro-positioning stage. It allows us to scan large and dense objects (Fig. 1).

The X-ray source voltage of the micro-CT scanner was set to 130 keV, the current was 61 μA and exposure time was equal

Table.1
Concrete and reinforced concrete mixes used in experiments.

| Mix components	Concrete	Concrete with industrial fibers	Concrete with recycled fibers
Cement (Portland CEM II/B-S 42.5N-NA)	320 kg/m^3	320 kg/m^3	320 kg/m^3
Sand (0–2 mm)	808 kg/m^3	794 kg/m^3	781 kg/m^3
Gravel aggregate (2–8 mm)	687 kg/m^3	680 kg/m^3	670 kg/m^3
Gravel aggregate (8–16 mm)	457 kg/m^3	453 kg/m^3	445 kg/m^3
Water	160 kg/m^3	160 kg/m^3	160 kg/m^3
Superplasticizer	3.2 kg/m^3	3.2 kg/m^3	3.2 kg/m^3
Industrial fibers	0 kg/m^3	25 kg/m^3	0 kg/m^3
Recycled fibers	0 kg/m^3	0 kg/m^3	50 kg/m^3
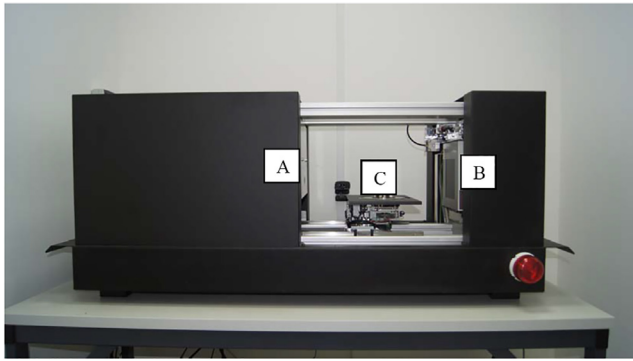
Fig. 1. Table 1173 Skyscan X-ray micro-tomograph: A) X-ray source, B) flat panel and C) precision object manipulator.

5000 ms. The pixel size of the micro-CT was 39.68 μm. The X-ray projections were recorded with the rotation increment of 0.2° within 360°. To reduce the noise in the captures X-ray projections, the frame averaging option was set to be 4 and random movement option was 10. The scanning time was approximately 12 h.

Fig. 2 presents a general view on cubic specimens 75 × 75 × 75 mm from images by 3D micro-CT. The heterogeneous 3D material micro-structure is well visible and the 3 phases (aggregate particles, cement matrix and air voids). In order to distinguish fibers and air voids from the concrete thresholding, which is based on the density of each material phase, should be performed. This procedure always makes some difficulties since the determination of the proper thresholding value in multi-phase materials is not unambiguous. In our experiments threshold in the range 245–255 and 0–60 was used for fibers and air voids respectively. Figs. 3

and 4 show 3D micro-CT images of steel fibers distribution (recycled and industrial) and distribution of air voids. Measured by micro-CT, total volume of recycled steel fibers (RSF) was 0.58% and total volume of air voids in sample was 1.73% (Fig. 3a and b) whereas total volume of industrial steel fibers (ISF) was 0.36% and total volume of air voids in sample was 2.76% (Fig. 4a and b). Total volume of air voids in plain concrete sample was 2.33%.

On the basis of micro-CT images one can measure diameter, volume, orientation and moments of inertia of fibers. The diameter of the fibers can be analysed using structure thickness 3D analysis which gives the average thickness (mean diameter) as well as the thickness distribution. Fibers length does not arise directly from the analysis. This has to be calculated on the basis of the diameter and volume of fibers. When one assumes the fibers to be cylinders, the development length can be easily achieved. Important note is that procedure works well when fibers are separated and are not touching each other in 3D. Otherwise, measurements and calculations can give some artifacts. Nevertheless, micro-CT is still powerful tool to measure fibers embedded in concrete since software gives some possibilities to separate fibers and make measurements more realistic.

Figs. 5 and 6 present results of micro-CT measurements of fiber diameter and development length in samples with industrial steel fibers (ISF) and recycled steel fibers (RSF), respectively. Measured diameter of industrial steel fibers varied mainly between $d_{lf} = 0.41$ mm and $d_{lf} = 0.53$ mm (Fig. 5a) whereas development length varied between $l_{d,lf} = 10$ mm and $l_{d,lf} = 29$ mm (Fig. 5b). Manufacturer declared fibers of diameter equal $d_{lf} = 0.50$ mm and length equal $l_{lf} = 25$ mm (not development length). Surprisingly, the distribution of diameters and development lengths obtained in micro-CT is quite wide which is not expected for industrial products. The scatter of fiber lengths is connected with the specimens
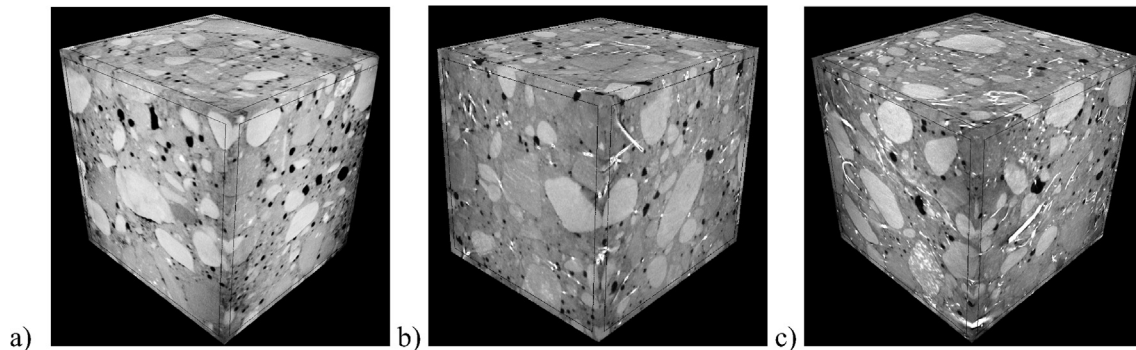

Fig. 2. General view on cubic specimens from images by 3D micro-CT: a) concrete, b) concrete reinforced with industrial fibers and c) concrete reinforced with recycled fibers.
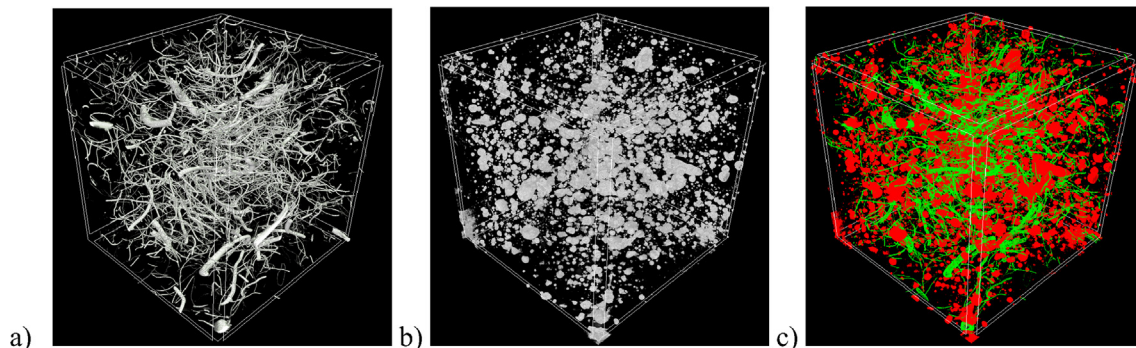

Fig. 3. 3D micro-CT images of the concrete reinforced with recycled fibers: a) distribution of steel fibers, b) distribution of air voids and c) combination of steel fibers (green) and air voids (red). (For interpretation of the references to color in this figure legend, the reader is referred to the web version of this article.)
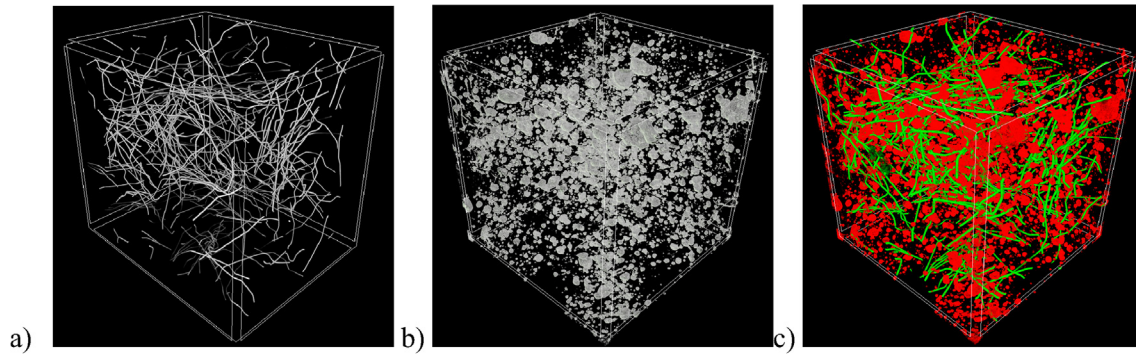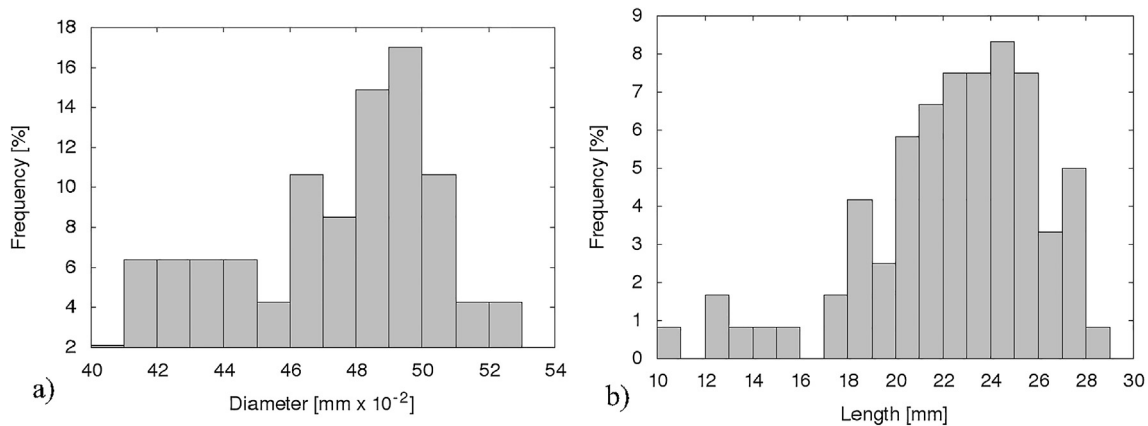
Fig. 4. 3D micro-CT images of the concrete reinforced with industrial fibers: a) distribution of steel fibers, b) distribution of air voids and c) combination of steel fibers (green) and air voids (red). (For interpretation of the references to color in this figure legend, the reader is referred to the web version of this article.)

Fig. 5. Industrial steel fibers measurements using micro-CT: a) frequency distribution of fiber diameter (d_{lf}) and b) frequency distribution of development length (l_{ld}).
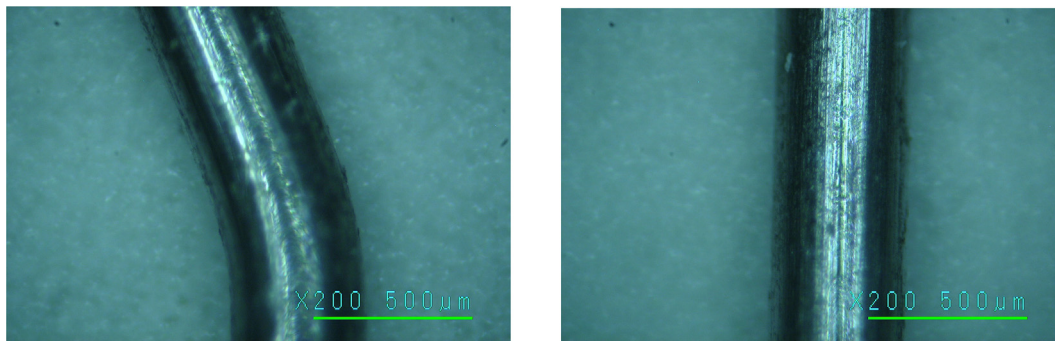

Fig. 6. Steel fiber of diameter equal 0.43 mm measured using digital microscope.

preparation. The cubes were cut out from single concrete block, therefore some fibers were cut on smaller pieces and their original length was decreased. On the other hand, fibers measured by micro-CT may be a bit longer since their length is measured along the fiber (with hooks) – on the basis of volume and diameter. To evaluate the results from micro-CT concerning fiber diameter distribution, we investigated steel fibers using digital microscope Scalar DG-3 with magnification ×200 times (Fig. 6). It turned out that fibers diameters are not always equal 0.5 mm. They differ within the range from 0.45 mm to 0.55 mm.

Measured diameter of recycled steel fibers varied mainly between d_{Rf} = 0.15 mm and d_{Rf} = 0.33 mm (Fig. 7a) whereas development length varied mainly between $l_{d,lf}$ = 5 mm and $l_{d,lf}$ = 40 mm (Fig. 7b). The distribution range of diameters (0.12–1.0 mm) and

lengths (2–100 mm) of recycled fibers is much wider than in case of industrial steel fibers, as the recycled fibers were not initially sorted. Fig. 8 presents structure thickness analysis that allows to visualise fibers diameters that are assigned different colour for the assumed diameter range.

Orientation of steel fibers is measured on the basis of the moments of inertia. Fig. 9 shows volume rendering image of fibers deviation from the vertical axis. It is measured in the range of 0°–90°. In case of industrial steel fibers: 12% were oriented within 0°–30°, 34% within the range 30°–60° and 54% within the range 60°–90°. In case of recycled steel fibers: 8% were oriented within 0°–30°, 30% within the range 30°–60° and 62% within the range 60°–90°. It means that the amount of RSF and ISF oriented horizontally is about 4.5–8 times larger than the amount of fibers oriented
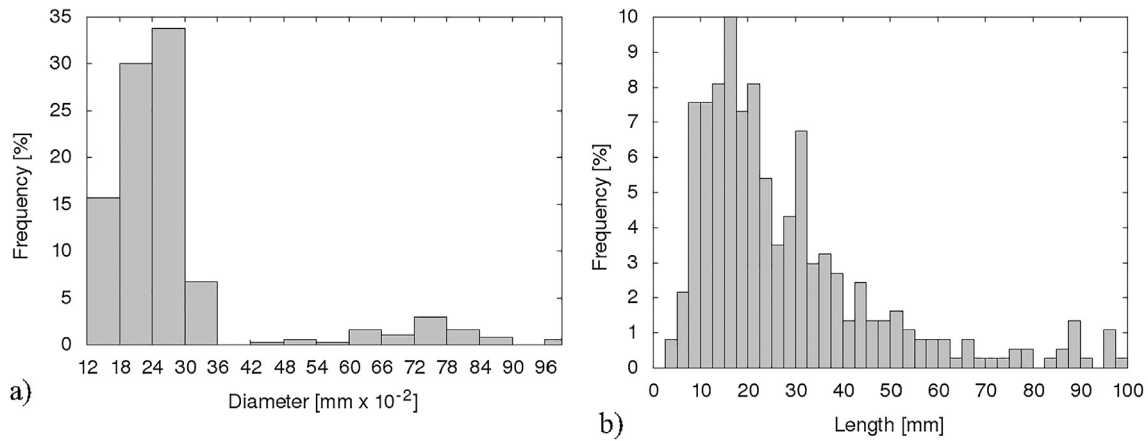
Fig. 7. Recycled steel fibers measurements using micro-CT: a) frequency distribution of fiber diameter (d_{lf}) and b) frequency distribution of development length (l_{ld}).
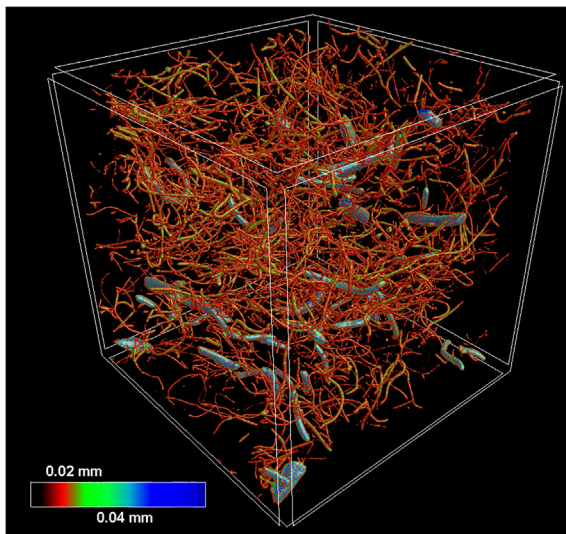

Fig. 8. Structure thickness analysis of recycle steel fibers diameter (d_{lf}).

vertically. It also means that fibers are more oriented in the direction of flowing mix. Similar but more emphasized tendency was observed by Ponikiewski et al. [60]. It can be noticed that orientation of the recycled and industrial steel fibers is very similar. The mean aspect ratio (relationship between diameter and development length) for industrial fibers was 60, whereas for recycled fibers it was 40. The distribution of aspect ratio for industrial fibers was very steep (more than 70% of fibers had aspect ratio in range 48–72), while for recycled fibers the distribution varied from 5 to 300 and only 40% of measurements were in range 34–58 (Fig. 10).

4. Mechanical properties of concrete and fiber-reinforced concrete

In order to characterize mechanical properties of recycled steel fiber reinforced concrete compressive strength, tensile splitting strength, shrinkage, tensile and residual strength in 3-point bending were analysed and compared to plain concrete and concrete reinforced with industrial steel fibers.

4.1. Compressive strength

For each mixture, six cubes ($150 \times 150 \times 150$ mm) were prepared. All tests were performed after 28 days of curing according
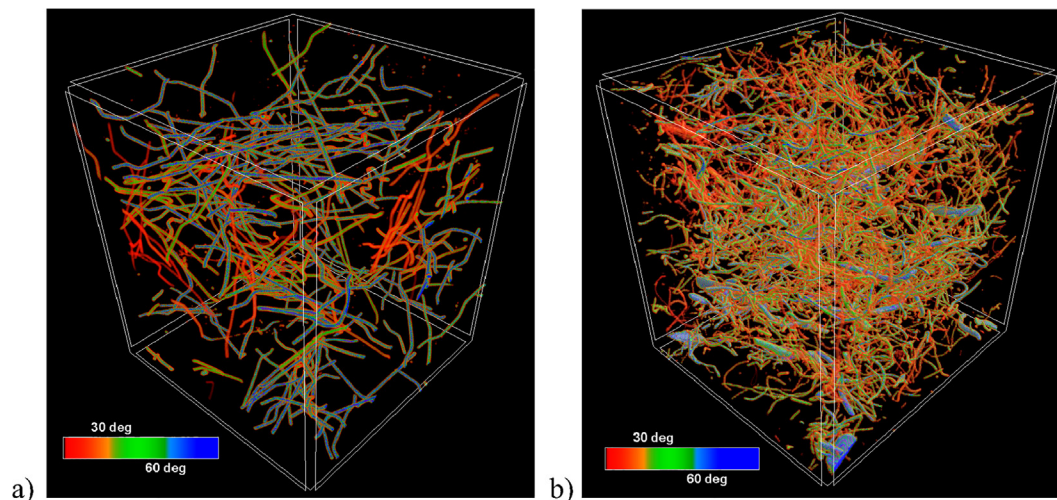

Fig. 9. Volume rendering image of: a) industrial steel fibers and b) recycled steel fibers in a concrete sample. Colours denote deviation of fibers from the vertical axis. (For interpretation of the references to colour in this figure legend, the reader is referred to the web version of this article.)
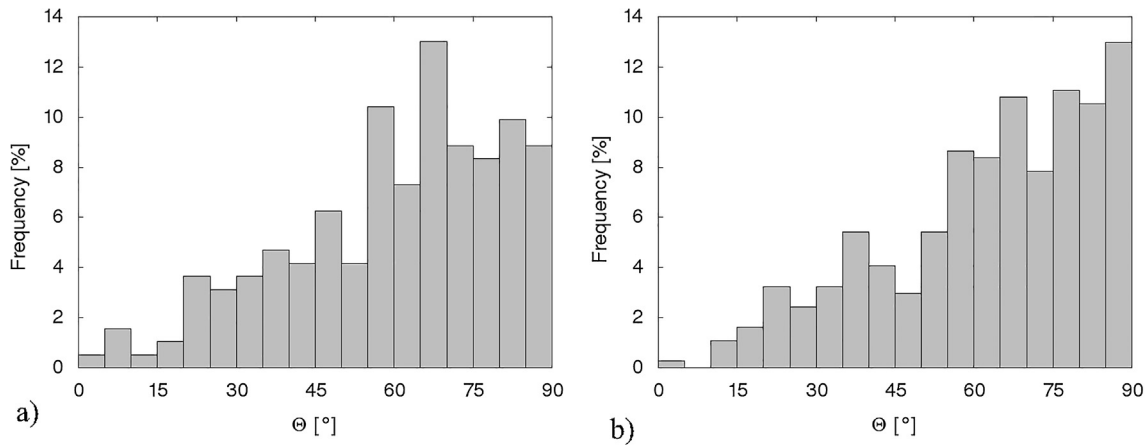
Fig. 10. Orientation of: a) industrial fibers and b) recycled fibers measured as deviation from the vertical axis.

to EN 12390-2:2009 standard [66] and procedure described in EN 12390-3:2009 [67]. Table 2 summarizes the results of the compression tests performed on cubic samples on plain and fiber reinforced concrete mixtures.

Mean compressive strength of plain concrete samples was equal σ_c = 42.91 MPa with the standard deviation of 2.27 MPa, mean strength of concrete reinforced with industrial fibers σ_{If} = 48.71 MPa with the standard deviation 1.29 MPa and mean strength of concrete reinforced with recycled fibers σ_{Rf} = 52.42 MPa with the standard deviation 2.48 MPa. The presence of the fibers leads to enhancing medium compressive strength between 13% (recycled fibers) and 22% (industrial fibers) in comparison to the corresponding plain mixture. Moreover, medium compressive strength of concrete reinforced with recycled fibers was higher for about 8% than concrete reinforced with industrial fibers. Li [68] and Caggiano [13] also observed that the presence of fibers slightly influences the compressive strength but only up 5–10%.

4.2. Tensile splitting strength

For each mixture, six cubes ($d = 150 \times 150 \times 150$ mm) were prepared. All tests were performed after 28 days of curing according to standard EN 12390-2:2009 [66] and procedure described in EN 12390-6:2011 standard [69]. The tensile splitting strength is given by the formulae:

$$f_{ct}^{spl} = \frac{2F}{\pi d^2} \tag{1}$$

where d is a side dimension of the tested cube. Table 3 summarizes the results of the compression tests performed on cubic sampled on both plain and fiber reinforced concrete mixtures.

Average tensile splitting strength of plain concrete samples was equal σ_c = 2.71 MPa with the standard deviation of 0.28 MPa, average strength of concrete reinforced with industrial fibers σ_{If} = 3.54 MPa with the standard deviation 0.25 MPa and average

Table 2
Failure force and compressive strength of concrete and fiber reinforced concrete.

Sample number	Concrete		Concrete with industrial fibers		Concrete with recycled fibers	
	Failure force F [kN]	Stress σ_c [MPa]	Failure force F [kN]	Stress σ_{If} [MPa]	Failure force F [kN]	Stress σ_{Rf} [MPa]
1	977.2	43.43	1054.1	46.85	1155.5	51.36
2	985.3	43.79	1097.0	48.76	1246.3	55.39
3	985.0	43.78	1115.2	49.56	1180.5	52.47
4	862.0	38.31	1093.1	48.58	1221.7	54.30
5	989.5	43.97	1078.4	47.93	1086.4	48.28
6	994.1	44.18	1137.8	50.57	1185.8	52.70
Average	**965.5**	**42.91**	**1095.9**	**48.71**	**1179.4**	**52.42**

Table 3
Failure force and tensile splitting strength of concrete and fiber reinforced concrete.

Sample number	Concrete		Concrete with industrial fibers		Concrete with recycled fibers	
	Failure force F [kN]	Stress σ_c [MPa]	Failure force F [kN]	Stress σ_{If} [MPa]	Failure force F [kN]	Stress σ_{Ef} [MPa]
1	107.9	3.05	123.1	3.48	141.7	4.01
2	105.8	2.99	110.0	3.11	146.8	4.15
3	91.8	2.60	134.7	3.81	138.6	3.92
4	82.7	2.34	131.3	3.72	127.7	3.61
5	89.2	2.52	122.3	3.46	125.6	3.55
6	96.6	2.73	129.0	3.65	140.6	3.98
Average	**95.7**	**2.71**	**125.1**	**3.54**	**136.8**	**3.87**

strength of concrete reinforced with recycled fibers σ_{Rf} = 3.87 MPa with the standard deviation 0.24 MPa. The presence of the fibers leads to enhancing average tensile splitting strength between 30% (industrial fibers) and 43% (recycled fibers) in comparison to the corresponding plain mixture. Moreover, average tensile splitting strength of concrete reinforced with recycled fibers was higher for about 9% than concrete reinforced with industrial fibers.

4.3. Shrinkage

Concrete shrinkage is one of the most unfavorable phenomenon occurring in concrete. It consists of spontaneous rheological deformations of cement paste as a result of the physico-chemical processes of water loss during binding, hardening and drying of concrete. Despite the fact that the aggregate during the shrinkage behaves passively, it is believed that presence of aggregate has an effect on reducing and slowing down shrinkage deformations in proportion to the amount of used aggregate [70]. The total shrinkage consists of autogenous (plastic) shrinkage as well as physical shrinkage due to drying out. Autogenous shrinkage occurs in the plastic state and is caused by the loss of water entering into chemical reaction with cement and its evaporation from the outer layers of the cement matrix. Autogenous shrinkage occurs only in the first hours but in the rapid way, whereas deformations from physical shrinkage increase much slower but in the long term, hence physical shrinkage determines the magnitude of the total shrinkage stress. Shrinkage causes tensile stress in concrete which can lead to the formation of cracks. The consequence of shrinkage cracks is a significant reduction in the durability of the structure.

In order to investigate shrinkage, for each mixture, 3 beams (100 × 100 × 500 mm) were prepared. Experimental tests were performed using Amsler apparatus according to the procedure described in Polish recommendations [71]. The test showed that after 112 days of maturation, the plain concrete achieved a shrinkage of 0.205‰, the concrete with industrial steel fibers 0.225‰, whereas the concrete with fibers derived from the recycling of tyres obtained a shrinkage value of 0.220‰ (Fig. 11). Although shrinkage was not improved by the addition of fibers, a close convergence was observed. Similar phenomenon was observed in tests by Dehghan et al. [72] and Noushini et al. [73]. This means that both fresh plain and fresh fiber reinforced concrete should be properly cured at early stages of hardening in order to preserve shrinkage cracking.

4.4. Three-point bending test

In the case of composites reinforced with fibers, the determination of the residual tensile strength in bending is a key test, which
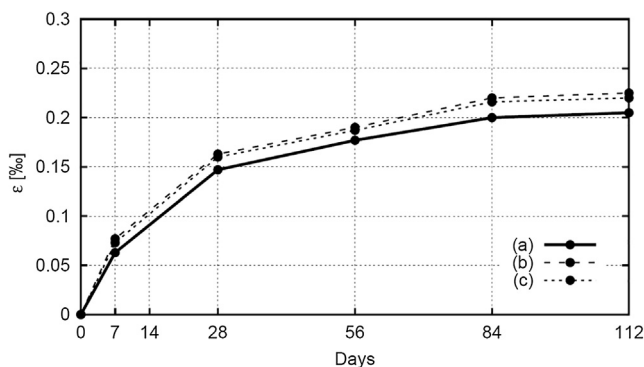
is used in the calculations of structural elements according to RILEM recommendations [74]. The addition of fibers plays a role similar to the bar reinforcement in concrete, fibers transfer stresses in the tensile zone after occurrence of the first crack.

The tensile behavior of fiber concrete is evaluated in terms of residual flexural tensile strength values determined from the load-CMOD curve obtained by applying a centre-point load on a simply supported sample. Experimental tests were carried out according to EN 14651:2005 + A1:2007 standard [75]. The experimental program included three-point bending laboratory tests carried out on 3 beams of each type (concrete, concrete with industrial steel fibers, concrete with recycled steel fibers), with the rectangular cross-section. The width and depth of beams were 150 mm, a length was 700 mm and span length was 500 mm. A notch of the height of 25 mm and width of 5 mm was located at the mid-span of beams. The quasi-static deformation was controlled by a vertical displacement u prescribed at the top of the beams mid-span, whereas Crack Mouth Opening Displacement (CMOD) was measured using gauge placed in the notch. This type of control allowed for obtaining a steady strength decrease in a post-peak regime.

Limit of proportionality (LOP) is given by the expression [75]:

$$f_{ct,L}^f = \frac{3F_L l}{2bh_{sp}^2} \tag{1}$$

where F_L is the load corresponding to the LOP (the highest load value in the interval of 0.05 mm of CMOD), l is the span length, b is the width of the specimen and h_{sp} is the distance between the tip of the notch and the top of the specimen. The residual flexural tensile strength is given by the following expression [75]:

$$f_{R,j} = \frac{3F_j l}{2bh_{sp}^2} \tag{2}$$

where F_j is the load corresponding to CMOD$_j$. The residual flexural tensile strength is calculated for CMOD$_1$ = 0.5 mm, CMOD$_2$ = 1.5 mm, CMOD$_3$ = 2.5 mm and CMOD$_4$ = 3.5 mm.

Fig. 12 shows the experimental curves of the vertical force F versus CMOD and Table 4 summarizes the experimental results. Visible effect of fiber presence was observed. Plain concrete shows low ductility in the softening regime and failed before CMOD = 0.1 mm was reached. Average limit of proportionality (LOP) was equal to 4.28 MPa for industrial steel fibers and 4.67 MPa for recycled steel fibers. These values are higher for about 20% and 30% respectively, in comparison to plain concrete. The average residual flexural tensile strength of samples reinforced with recycled steel fibers were equal $f_{R,0.5}$ = 2.45 MPa and $f_{R,2.5}$ = 1.26 MPa and were higher for about 7% ($f_{R,0.5}$ = 2.29 MPa) and for about 38% ($f_{R,2.5}$ = 0.91 MPa) than the average residual flexural strength of samples reinforced with industrial steel fibers.

5. Fracture properties

5.1. Experimental procedure

To visualise fracture process zone development an unique test stand has been built. It consists of ISTRON 5569 static machine with the maximum force 50 kN and SkyScan 1173 micro-CT mounted on it. Micro-CT can be move up and down on the machine frame. To rotate the sample a rotating frame and stepper rotor are used (they can be controlled from the micro-CT software) (Figs. 13 and 14). This stand allows us to continuously observe sample micro-structure during the deformation process. There are two possible ways of scanning:
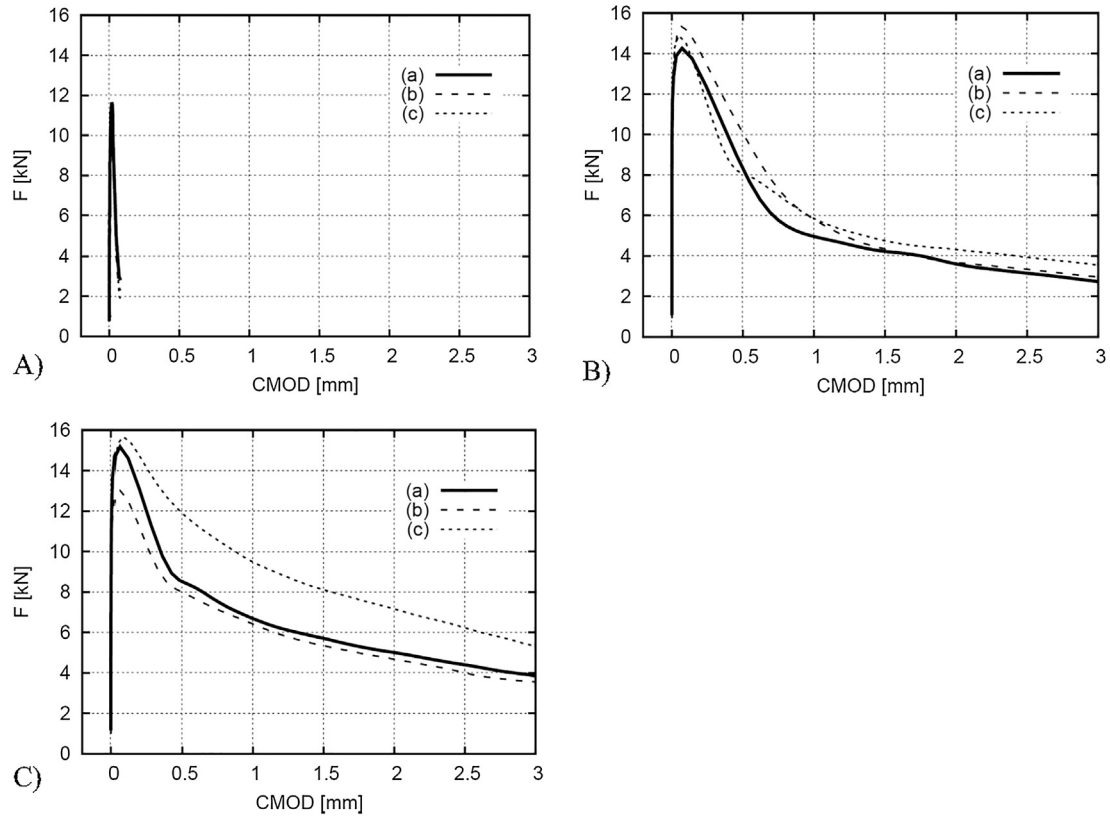

Fig. 11. Shrinkage strain evolution: a) concrete, b) concrete with industrial fibers and c) concrete with recycled fibers.

Fig. 12. Experimental force-CMOD diagrams for 3 samples of each type (curves (a)–(c)): A) plain concrete, B) concrete reinforced with industrial steel fibers and C) concrete reinforced with recycled steel fibers.

Table 4
Limit of proportionality force and three-point bending strength of concrete and fiber reinforced concrete.

Sample number	Concrete		Concrete with industrial fibers				Concrete with recycled fibers			
	LOP F_L [kN]	$f^f_{ct,L}$ [MPa]	LOP F_L [kN]	$f^f_{ct,L}$ [MPa]	$f_{R,0.5}$ [MPa]	$f_{R,2.5}$ [MPa]	LOP F_L [kN]	$f^f_{ct,L}$ [MPa]	$f_{R,0.5}$ [MPa]	$f_{R,2.5}$ [MPa]
1	11.65	3.73	14.85	4.75	2.08	0.85	15.12	4.84	2.14	1.08
2	11.36	3.64	15.24	4.88	2.64	0.90	13.21	4.23	2.02	1.04
3	10.60	3.39	15.12	4.82	2.14	0.98	15.42	4.93	3.20	1.67
Average	**11.20**	**3.59**	**15.05**	**4.82**	**2.29**	**0.91**	**14.58**	**4.67**	**2.45**	**1.26**

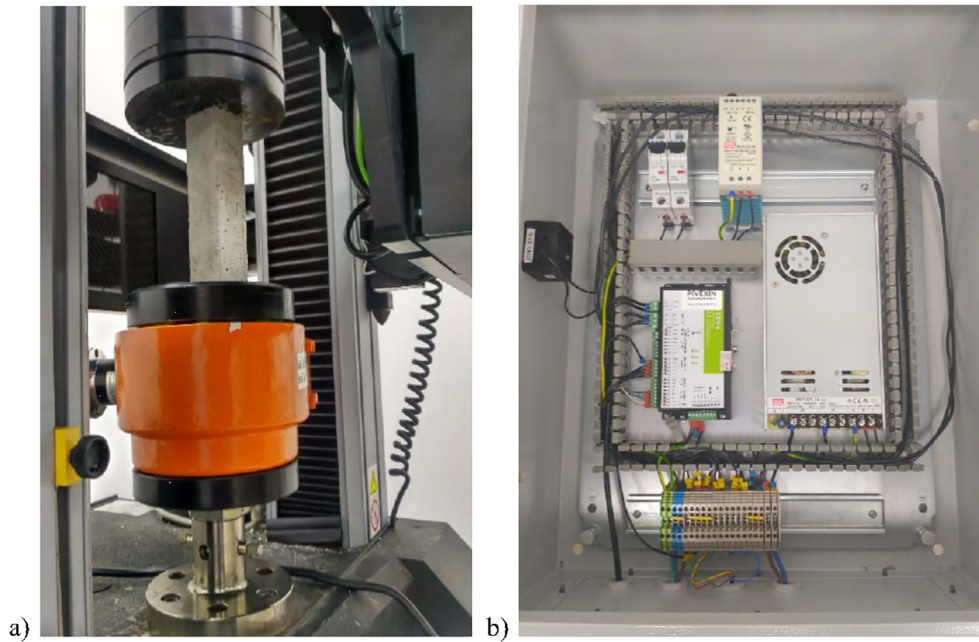**Fig. 13.** Micro-CT Skyscan 1173 mounted on an Instron 5569 quasi-static machine.

Fig. 14. Micro-CT mounted on INSTRON 5569: a) rotating frame and b) stepper rotor.

1. **Stop and scan**: after a certain load level is reached, deformation process is stopped and force is kept constant. Micro-CT makes first image then send signal to stepper to rotate sample. After rotation is finished, micro-CT makes a second image etc.
2. **Scan continuously**: micro-CT scans sample during the deformation process without stopping the machine. To obtain scans of well quality, deformation process should be very slow (up to several hours). Procedure of scanning is the same as in a previous option.

In our experiments second option of scanning was used. In order to use our system for constant observation of fracture process zone development the most suitable test is wedge splitting. The WST method has the advantage using a relatively small and compact specimen that was crucial since the sample should be visible in the field of view of the micro-CT system. Furthermore, the test method is stable and proved reliable for fracture testing of concrete. The wedge splitting test was developed in 1986 by Linsbauer and Tschegg [76] and since then has been widely used to identify the fracture mechanical properties of brittle and quasi-brittle material under mode I loading [77,78]. Our wedge splitting tests were carried out on cubic specimens 75 × 75 × 75 mm (characterised in detail in Section 2) placed on the linear steel support. The initial notch of the height of 10 mm and width of 5 mm was located at the middle of the sample. The quasi-static tests were performed with a controlled displacement rate of 0.002 mm/min whereas Crack Mouth Opening Displacement (CMOD) gauge was placed in the notch. This type of control allowed for obtaining a steady strength decrease in a post-peak regime. Initially fracture process zone development was investigated only on the surface of samples using Digital Image Correlation. The digital camera NIKON D800 with the 36 megapixel resolution was mounted on the tripod with its axis perpendicular to the photographed specimen surface. The surface of concrete samples was initially carefully polished and painted white. Next, a speckle pattern (serving as a tracer) was put on this surface using a yellow-black colour spray. The experimental set-up during DIC tests is presented in Fig. 15.
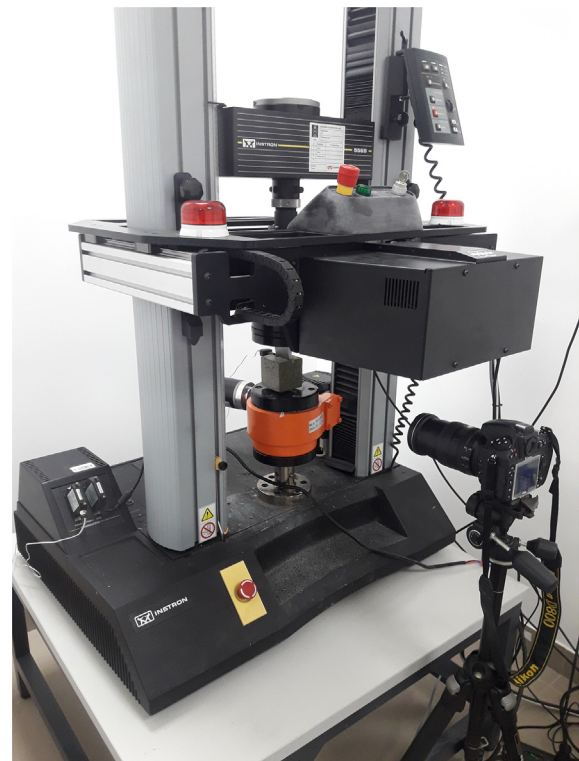

Fig. 15. Experimental set-up of wedge splitting test with SkyScan 1173 micro-CT mounted on INSTRON 5569, digital camera and CMOD gauge placed in the sample notch. (For interpretation of the references to colour in this figure legend, the reader is referred to the web version of this article.)

5.2. Characterization of the fracture process by Digital Image Correlation

In our experimental program, the digital images were continuously shot every 6 s during each test. One pixel of the taken photo
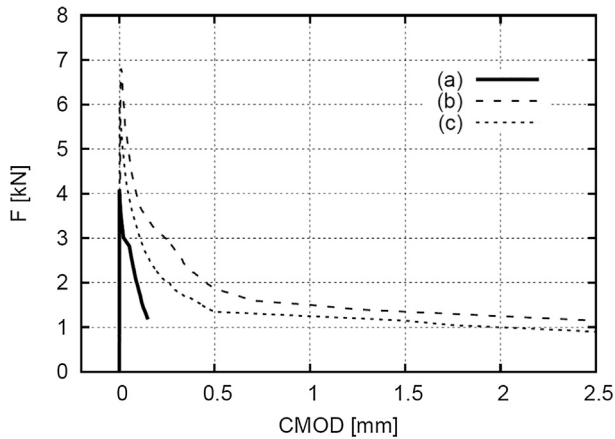
Fig. 16. Experimental forces-CMOD curves in wedge splitting test: a) plain concrete, b) concrete reinforced with industrial steel fibers and c) concrete reinforced with recycled steel fibers.

represented approximately the square of 18 μm on the cube surface and the length resolution was about 60 pixel/mm. The subset size 120 pixels was assumed to be bigger at least by 1 pixel than the biggest speckle used i.e. ≥60 pixels and distance between subset centres was 5 pixels [34,36].

Fig. 16 presents the experimental curves of the vertical force F versus CMOD (up to 2.5 mm) for plain concrete, concrete reinforced with industrial and recycled steel fibers. All measured vertical force-CMOD curves have the same slope in the entire elastic regime and are different after the peak load when fracture occurs (due to concrete heterogeneity and presence of steel fibers). The maximum force in plain concrete was equal to 4.07 kN and was about 70% smaller than maximum force measured in steel reinforced concrete which was equal about 6.80 kN for both ISF and RSF. Residual vertical forces in ISF reinforced concrete were $F_{res,0.5} = 1.78$ kN (at CMOD = 0.5 mm), $F_{res,1.5} = 1.29$ kN (at CMOD = 1.5 mm) and $F_{res,2.5} = 1.13$ kN (at CMOD = 2.5 mm) whereas residual vertical forces in RSF reinforced concrete were $F_{res,0.5} = 1.30$ kN (at CMOD = 0.5 mm), $F_{res,1.5} = 1.13$ kN (at
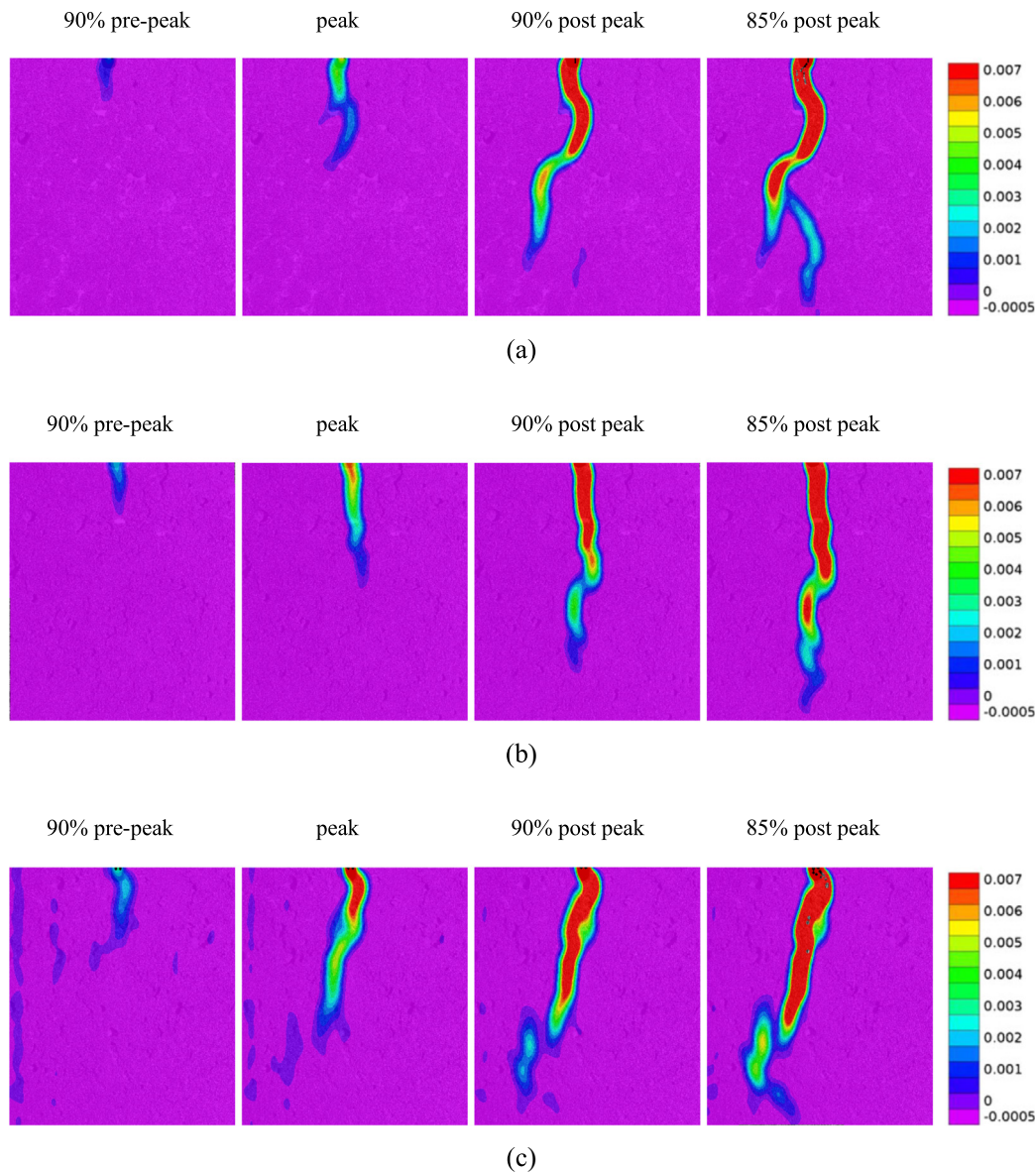

(a)

(b)

(c)

Fig. 17. Evolution of fracture directly under notch at different loading stages (Fig. 16) in DIC experiments of: a) plain concrete, b) concrete reinforced with ISF and c) concrete reinforced with RSF (colour scale denotes horizontal normal strain intensity). (For interpretation of the references to colour in this figure legend, the reader is referred to the web version of this article.)

CMOD = 1.5 mm) and $F_{res,2.5}$ = 1.08 kN (at CMOD = 2.5 mm). A fracture zone was always created before the peak on the vertical force-CMOD diagram at about 90% of the peak force in the pre-peak regime (Fig. 17). It might appear as a single slightly curved zone (Fig. 17b and c) or a tortuous branched zone (Fig. 17a).

Evolution of the fracture process zone can be also observed on the strain and displacement profiles. Maximum observed normal strain was in the range 0.035–0.075 and maximum horizontal displacements were in the range 0.105–0.11 mm.

To calculate the width of the fracture zone, surface strains calculated from the displacements (Fig. 18) were fitted by the usual normal distribution (Gauss) function and the standard deviation σ was calculated. The width of the fracture zone was calculated according to a following formulae [31]:

$$w_c = 4.0 \times \sigma. \tag{3}$$

Thus, 95% of the values of the normal distribution function area were within the distance of 2 standard deviations in both directions from the mean value. The width and length of the fracture zone (measured just under the notch) in concrete samples varied from w_c = 3.14 mm, l_c = 10.04 mm (Fig. 16a, 90% pre peak) to w_c = 4.85 mm, l_c = 57.60 mm (Fig. 16a, 85% post peak), in concrete reinforced with ISF varied from w_c = 2.86 mm, l_c = 12.09 mm (Fig. 16b, 90% pre peak) to w_c = 3.88 mm, l_c = 59.64 mm (Fig. 16b, 85% post peak) and in concrete reinforced with RSF varied from w_c = 2.84 mm, l_c = 18.36 mm (Fig. 16c, 90% pre peak) to w_c = 3.89 mm, l_c = 61.21 mm (Fig. 16b, 85% post peak). The measured width of the fracture zone in plain concrete was about 25% larger than in concrete reinforced with industrial and recycled steel fibers. It shows that steel fibers have the ability of limiting micro-cracking area.
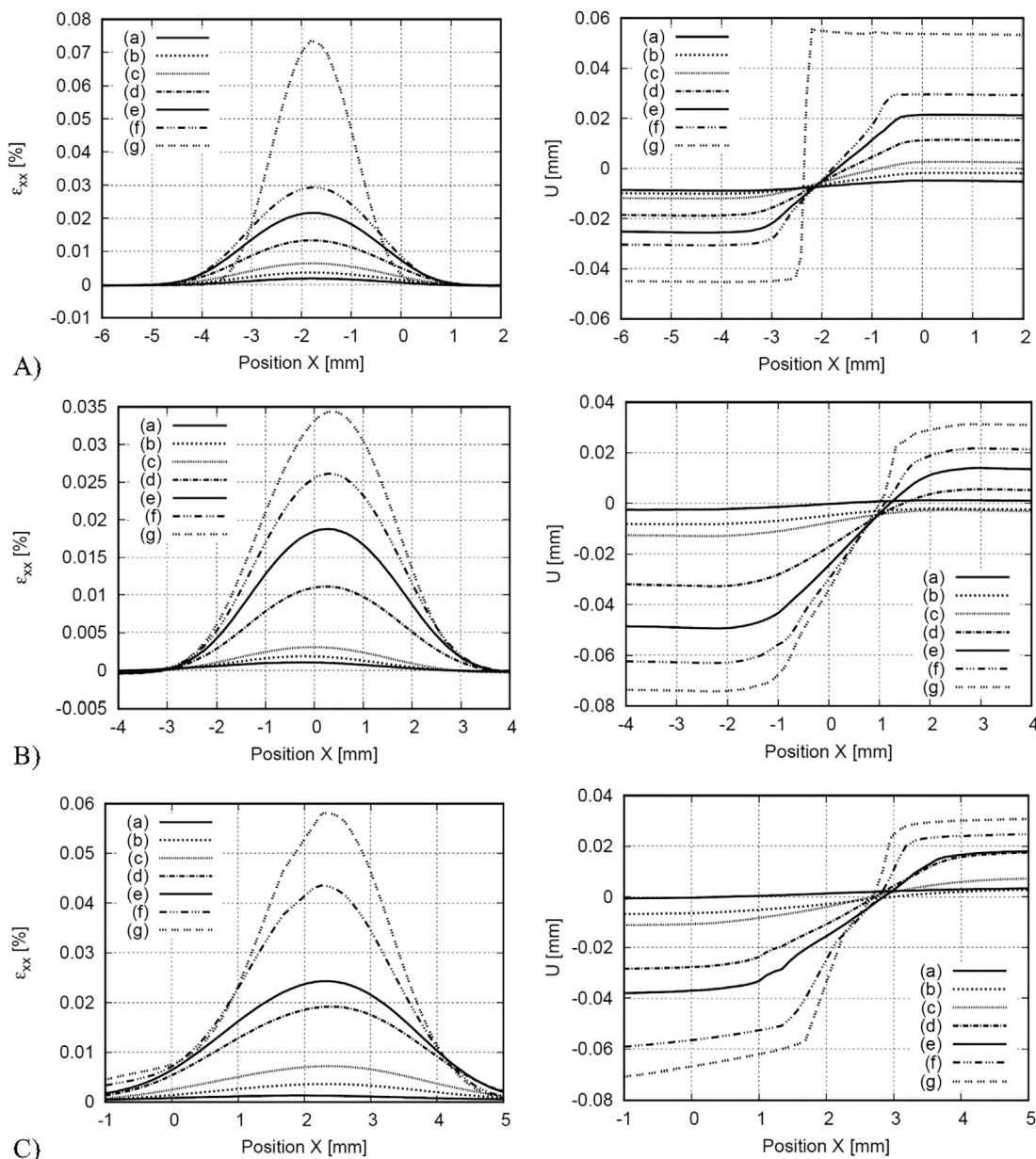

Fig. 18. Measurement of evolution of the fracture process zone under the notch: strain profile (left column) and displacement profile (right column) from experiments using DIC for a) 85% pre peak, b) 90% pre peak, c) 95% pre peak, d) peak, e) 90% post peak, f) 85% post peak (before macro-crack formation): A) plain concrete, B) concrete reinforced with industrial steel fibers and C) concrete reinforced with recycled steel fibers.

5.3. Characterization of the fracture process by micro-CT

To investigate fracture zone in 3D a micro-CT was used. Before each experiment an initial scan was performed (see Section 3). Next, during the deformation process several other scans were done, mainly close to the peak and in the post-peak softening regime. Since the deformation process was continuous, it was crucial to minimize scanning time but simultaneously preserve image quality. In order to fulfill these both requirements, several preliminary scannings were carried out. Thus, the X-ray source voltage of the micro-CT scanner was finally set to 130 keV, the current was 61 μA and exposure time was equal 400 ms. The pixel size of the micro-CT was 39.68 μm. The X-ray projections were recorded with

the rotation increment of 0.4° within 360°. To reduce the noise in the captures X-ray projections, the frame averaging option was set to be 2 and random movement option was 4. The single scanning time was approximately 1 h. Figs. 19–21 present 3D images from micro-CT of samples scanned at different loading stages. The crack is strongly curved due to presence of aggregate grains and air voids. The crack mainly propagate close to the aggregate grains in the interfacial transition zones (contact zones between the cement matrix and aggregate) which are the weakest phase in concrete [79,80]. However, sometimes crack propagates through the aggregate grain.

Fig. 22 presents the comparison between the fracture process zone obtained by DIC technique on the surface of the specimens
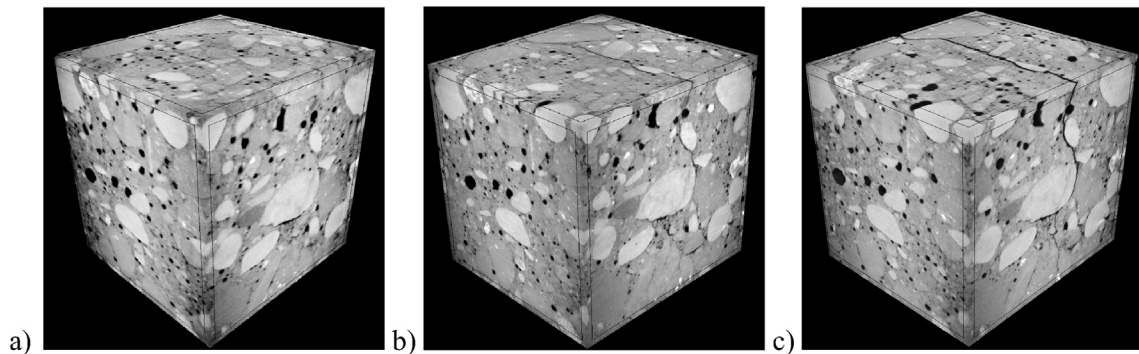

Fig. 19. General view on concrete cubic specimens from images by 3D micro-CT: a) non-cracked before WST test, b) cracked, at CMOD = 0.06 mm c) cracked, at CMOD = 0.10 mm.
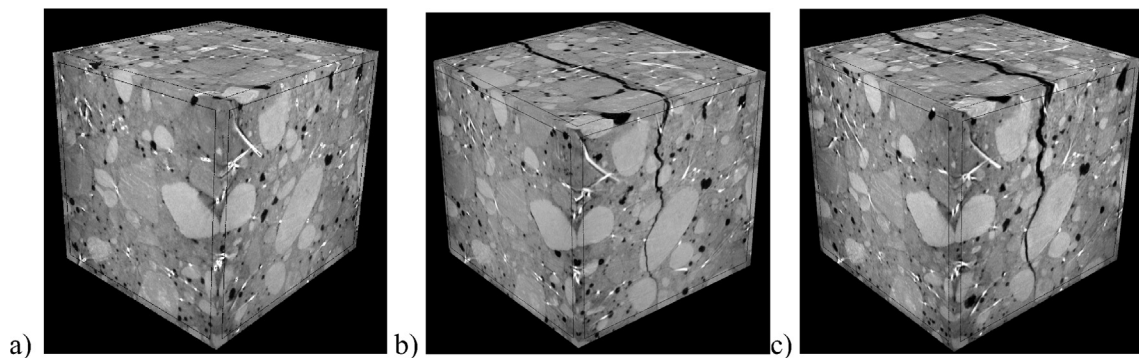

Fig. 20. General view on concrete reinforced with ISF cubic specimens from images by 3D micro-CT: a) non-cracked, before test, b) cracked, at CMOD = 1.5 mm c) cracked, at CMOD = 2.5 mm.
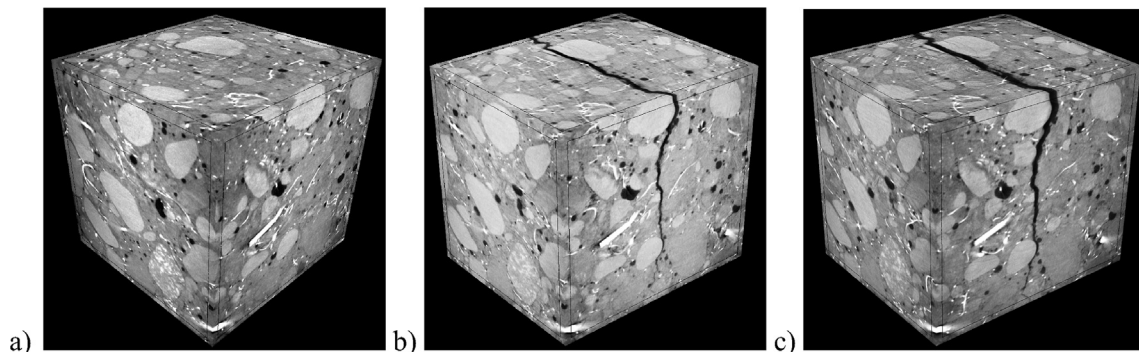

Fig. 21. General view on concrete reinforced with RSF cubic specimens from images by 3D micro-CT: a) non-cracked, before test, b) cracked, at CMOD = 1.5 mm c) cracked, at CMOD = 2.5 mm.
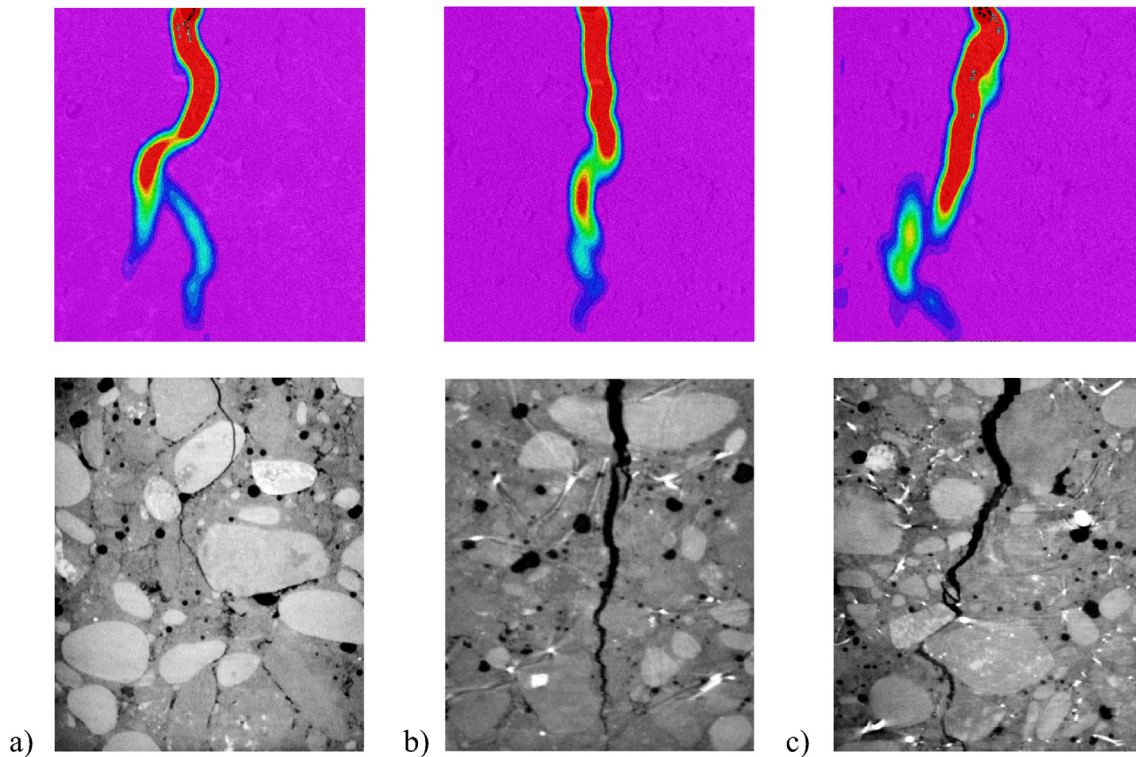
Fig. 22. Comparison of the fracture zone observed on the surface of: a) concrete, b) concrete reinforced with ISF and c) concrete reinforced with RSF observed at the 85% of the post peak load with micro-CT images of cracked samples at the end of the test.

before the macro-crack appeared and images from micro-CT taken at the end of each test (after the macro-crack appeared and evolved). It can be noticed that DIC realistically captured the shape of the fracture process zone that is the predecessor of the crack. Fig. 23 shows the 3D visualisation of the crack in concrete reinforced with ISF and RSF. It is visible that crack area is strongly curved along sample depth and its width is non-uniform. Crack width is presented using colour scale. The crack width non-linearly changes along depth and height of the

specimen due to random distribution of aggregate grains, air voids and steel fibers.

In concrete reinforced with RSF, the crack surface area is equal 15,259.1 mm^2 and its volume is 4062.1 mm^3. Crack makes up 2.0% of the scanned sample. In concrete reinforced with ISF, the crack surface area is equal 15,119.4 mm^2 and its volume is 3888.7 mm^3. Crack makes up 1.8% of the scanned sample.

Figs. 24 and 25 show a 3D visualisation of crack as well as distribution of ISF and RSF. Both type of fibers are crossing the crack
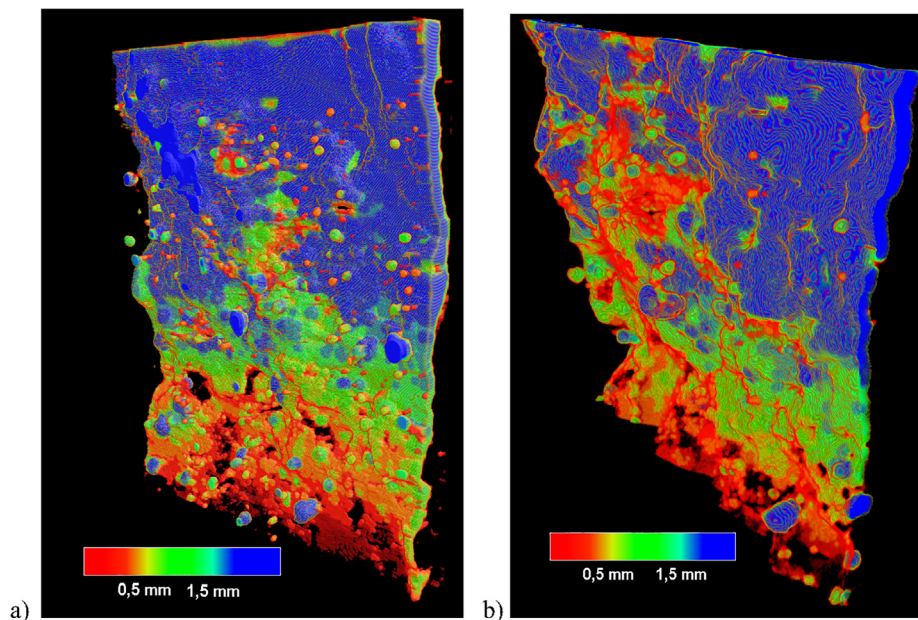

Fig. 23. Crack width distribution in concrete reinforced with: a) industrial steel fibers and b) recycled steel fibers by micro computed tomography at CMOD=2.5 mm of Fig. 16.
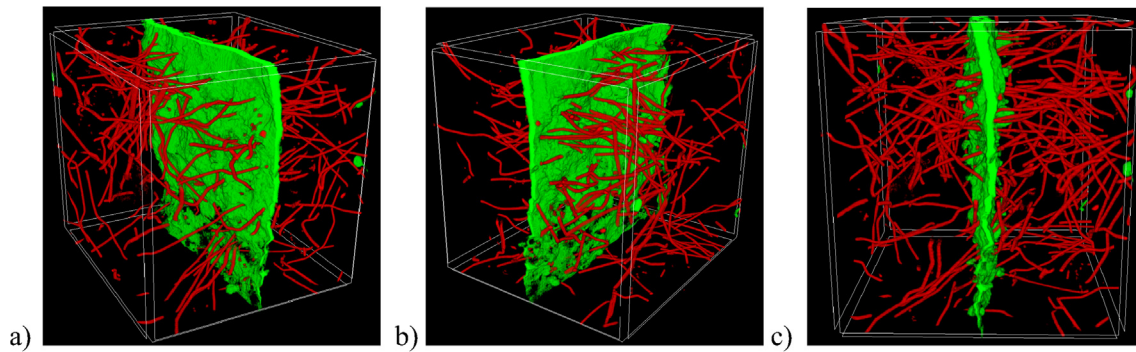
Fig. 24. Different views of ISF (red) crossing macro-crack (green): a), b) side views and c) front view at CMOD = 2.5 mm of Fig. 15. (For interpretation of the references to color in this figure legend, the reader is referred to the web version of this article.)

Fig. 25. Different views of RSF (red) crossing macro-crack (green): a), b) side views and c) front view at CMOD = 2.5 mm of Fig. 15. (For interpretation of the references to color in this figure legend, the reader is referred to the web version of this article.)
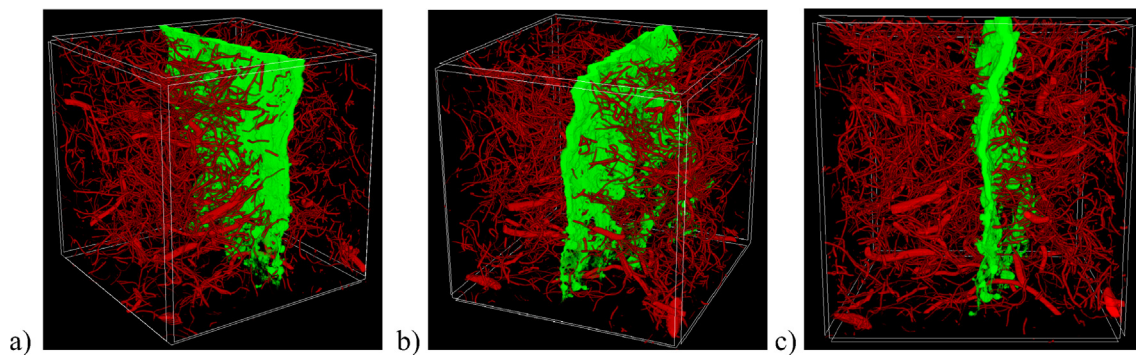
and are able to limit its opening that leads to the increase of ductility and durability of structural concrete components.

6. Conclusions

This paper presents the results of an experimental research aimed at mechanical properties and determination of the fracture process zone development in concrete reinforced with both ISF and RSF in comparison to the plain concrete. Non-destructive observations using optical method called Digital Image Correlation and X-ray micro computed tomography were carried out. The following conclusions can be drawn:

- Recycled steel fibers (RST) recovered from end-of-life tyres can be considered as the valuable eco-friendly reinforcement of concrete intended for industrial floors. Strengthening concrete matrix with inhomogeneous recycled fibers (RSF), made of high quality steel, improves concrete mechanical properties such as: compressive strength, tensile strength, residual strength and crack-bridging which preserves load capacity and durability of the structure.
- Measured by X-ray micro-CT diameter of used recycled steel fibers (RSF) varied mainly between $d_{Rf} = 0.15$ mm and $d_{Rf} = 0.33$ mm whereas the development length varied mainly between $l_{d,lf} = 5$ mm and $l_{d,lf} = 40$ mm. The total distribution range of diameters (0.12–1.0 mm) and lengths (2–100 mm) of RSF is much wider than in case of ISF, as the recycled fibers were not initially sorted.
- As the recycled fibers have very differentiated lengths, diameters and aspect ratio (fibers were not initially sorted in terms of diameter and length) some of them are passive in fracture

process. This means that to obtain similar RSF and ISF reinforced concrete capacity and durability properties, RSF amount should be twice more.
- On the basis of X-ray micro-CT measurements it turned out that 8% of RSF embedded in concrete matrix were oriented (deviation from the vertical axis) within 0–30° (vertical orientation), 30% within the range 30°–60° and 62% within the range 60°–90° (horizontal orientation). It means that the amount of fibers oriented horizontally is about 8 times larger than the amount of fibers oriented vertically. It also means that fibers are more oriented in the direction of flowing mix. Similar tendency was observed for ISF.
- Presence of RSF (50 kg/m³, 0.25%), enhanced both the compressive strength by about 22% and the tensile splitting strength by about 43% in comparison to the corresponding plain mixture. In comparison to concrete reinforced with ISF (25 kg/m³, 0.25%), presence of RSF, increased compressive strength for about 8% and the tensile splitting strength for about 9%.
- Presence of RSF (50 kg/m³, 0.25%), enhanced average residual flexural tensile strength by about 7% ($f_{R,0.5}$) and by about 38% ($f_{R,2.5}$) in comparison to the mixture reinforced with ISF (25 kg/m³, 0.25%).
- Shrinkage after 112 days of concrete with RSF and ISF was equal 0.220‰, 0.225‰, respectively. Shrinkage of plain concrete was equal 0.205‰. Thus, the shrinkage phenomenon was not improved by presence of RSF and ISF, however a close convergence was observed. This means that both fresh plain and fresh fiber reinforced concrete should be properly cured at early stages of hardening in order to preserve shrinkage cracking.
- All measured, in wedge splitting test (WST), vertical force-CMOD curves have the same slope in the entire elastic regime

and are different after the peak load when fracture occurs (due to concrete heterogeneity and presence of steel fibers). The maximum force in plain concrete was about 70% smaller than maximum force measured in steel reinforced concrete for both industrial and recycled steel fibers.

- DIC technique realistically captured shape of the fracture process zone that is the predecessor of the crack. A fracture process zone was always created before the peak on the vertical force-CMOD diagram after about 90% of the peak force in the pre-peak regime. It might appear as a single slightly curved zone or a tortuous branched zone.
- Both ISF and RSF are able to limit micro-cracking area and macro-crack opening under loading. The measured width of the fracture zone in plain concrete was about 25% larger than in concrete reinforced with ISF and RSF.
- On the basis of continuous X-ray micro-CT measurements of ISF and RSF reinforced concrete during the deformation process it was observed that the crack area is strongly curved along sample depth and its width is non-uniform. At final stage of loading (CMOD = 2.5 mm), in concrete reinforced with RSF, the crack surface area is equal 15,259.1 mm^2 and its volume is 4062.1 mm^3. Crack makes up 2.0% of the scanned sample. In concrete reinforced with ISF, the crack surface area is equal 15,119.4 mm^2 and its volume is 3888.7 mm^3. Crack makes up 1.8% of the scanned sample. It means that both types of fibers have similar ability of crack-bridging.

Conflict of interest

None.

Acknowledgements

References

[1] Z. Bažant, J. Planas, Fracture and Size Effect in Concrete and Other Quasi-Brittle Materials, CRC Press LLC, Boca Raton, 1997.

[2] G. Lilliu, J.G.M. van Mier, 3D lattice type fracture model for concrete, Eng. Fract. Mech. 70 (2003) 927–941.

[3] Ł. Skarżyński, M. Nitka, J. Tejchman, Modelling of concrete fracture at aggregate level using FEM and DEM based on X-ray μCT images of internal structure, Eng. Fract. Mech. 147 (2015) 13–35.

[4] A.-L. Hoang, E. Fehling, Influence of steel fiber content and aspect ratio on the uniaxial tensile and compressive behavior of ultra high performance concrete, Constr. Build. Mater. 153 (2017) 790–806.

[5] J.-H. Lee, B. Cho, E. Choi, Flexural capacity of reinforced concrete with a consideration of concrete strength and fiber content, Constr. Build. Mater. 138 (2017) 222–231.

[6] D.-Y. Yoo, Y.-S. Yoo, N. Banthia, Flexural response od steel-fiber-reinforced concrete beams: effect of strength, fiber content and strain-rate, Cem. Concr. Compos. 64 (2015) 84–92.

[7] Z. Wu, C. Shi, W. Hi, L. Wu, Effects of steel fibres distribution on mechanical properties of ultra high performance concrete, Constr. Build. Mater. 103 (2016) 8–14.

[8] M.N. Soutsos, T.T. Le, A.P. Lampropoulos, Flexural performance of fibre reinforced concrete made with steel and synthetic fibers, Constr. Build. Mater. 36 (2012) 704–710.

[9] J.M. Yang, K.H. Min, H.O. Shin, Y.S. Yoon, Effect of steel and synthetic fibers on flexural behaviour of high strength concrete beams reinforced with FRP bars, Compos. B Eng. 43 (3) (2012) 1077–1086.

[10] A. Caggiano, S. Gambarelli, E. Martinelli, N. Nistricò, M. Pepe, Experimental characterization of the post-cracking response in Hybrid Steel/Polypropylene Fiber-Reinforced Concrete, Constr. Build. Mater. 125 (2016) 1035–1043.

[11] A. Mada, F. Minelli, G.A. Plizzari, Flexural behaviour of RC beams in fiber reinforced concrete, Compos. B Eng. 43 (2012) 2930–2937.

[12] A. Caggiano, H. Xargay, P. Folino, E. Martinelli, Experimental and numerical characterization of the bond behaviour of steel fibers recovered from waste tyres embedded in cementitious matrices, Cem. Concr. Compos. 62 (2015) 146–155.

[13] A. Caggiano, P. Folino, C. Lima, E. Martinelli, M. Pepe, On the mechanical response of Hybrid Fiber Reinforced Concrete with Recycled and Industrial Steel Fiber, Constr. Build. Mater. 147 (2017) 286–295.

[14] A. Caggiano, G. Etse, E. Martinelli, Interface model for fracture behaviour of Fiber Reinforced Concrete Composites (FRCCs): theoretical formulation and numerical implementation, Eur. J. Environ. Civ. Eng. 15 (9) (2011) 1339–1359.

[15] O. Sengul, Mechanical behaviour of concretes containing waste steel fibers recovered from scrap tyres, Constr. Build. Mater. 122 (2016) 649–658.

[16] M. Leone, G. Centonze, D. Colonna, F. Micelli, M.A. Aiello, Fiber-reinforced concrete with low content of recycled steel fiber: shear behaviour, Constr. Build. Mater. 161 (2018) 141–155.

[17] K.M. Nemati, Fracture analysis of concrete using scanning electron microscopy, Scanning 19 (1997) 426–430.

[18] R.V. Balendran, H.W. Pang, H.X. Wen, Use of scanning electron microscopy in concrete studies, Struct. Surv. 16 (1998) 146–153.

[19] S.H. Hadjab, M. Chabaat, J.F. Thimus, Use of Scanning Electron microscope and the non-local isotropic damage model to investigate fracture process zone in notched concrete beams, Exp. Mech. 47 (2007) 473–484.

[20] J. Bhargava, A. Rehnström, High speed photography for fracture studies of concrete, Cem. Concr. Res. 5 (1975) 239–248.

[21] J.A. Leendertz, Interferometric displacement measurement on scattering surfaces utilizing speckle effect, J. Phys. E: Sci. Instrum. 3 (1970) 214–218.

[22] P. Jacquot, J.M. Fournier, Interferometry in Speckle Light: Theory and Applications, Springer, Berlin, 2000.

[23] A. Maji, C. Ouyang, S.P. Shah, Fracture mechanisms of concrete based on acoustic emission, J. Mater. Res. 5 (1990) 206–217.

[24] H. Mihashi, N. Nomura, Correlation between characteristics of fracture process zone and tension-softening properties of concrete, Nucl. Eng. Des. 165 (1996) 359–376.

[25] A. Carpinteri, G. Lacidogna, Damage diagnostic in concrete and masonry structures by acoustic emission technique, Autom. Control Robot. 3 (2003) 755–764.

[26] K. Otsuka, H. Date, Fracture process zone in concrete tension specimen, Eng. Fract. Mech. 65 (2000) 111–131.

[27] H. Hadjab, Fracture process zone in concrete beams: experimental investigation and numerical modelling, in: Proceedings of the SEM Annual Conference, June 1–4, Albuquerque New Mexico USA, 2009.

[28] G. Nagy, T. Zhang, W. Franklin, E. Landis, E. Nagy, D. Keane, Volume and surface area distributions of cracks in concrete, in: C. Arcelli, L.P. Cordella, G.S. di Baja (Eds.), Visual Form 2001, vol. 2059, 2001, pp. 759–768.

[29] E. Landis, E. Nagy, D. Keane, Microstructure and fracture in three dimensions, Eng. Fract. Mech. 70 (2003) 911–925.

[30] M.A.B. Promentilla, T. Sugiyama, X-ray microtomography of mortars exposed to freezing-thawing action, J. Adv. Concr. Technol. 8 (2010) 97–111.

[31] Ł. Skarżyński, J. Tejchman, Experimental investigations of fracture by means of X-ray micro computed tomography, Strain (2015), https://doi.org/10.1111/str.12168.

[32] S. Ri, M. Fujigaki, Y. Morimoto, Sampling Moiré method for accurate small deformation distribution, Measurement 50 (2010) 501–508.

[33] S. Ri, T. Muramatsu, M. Saka, K. Nanbara, D. Kobayashi, Accuracy of the sampling Moiré method and its application to deflection measurements of large-scale structures, Exp. Mech. 52 (2012) 331–340.

[34] D. Lecompte, A. Smits, S. Bossuyt, H. Sol, J. Vantomme, D. van Hemelrijck, A.M. Habraken, Quality assessment of speckle patterns for digital image correlation, Opti. Lasers Eng. 44 (2006) 1132–1145.

[35] G. Corr, M. Accardi, L. Graham-Brady, S. Shah, Digital image correlation analysis of interfacial debonding properties and fracture behavior in concrete, Eng. Fract. Mech. 74 (2007) 109–121.

[36] B. Pan, H. Xie, Z. Wang, K. Qian, Z. Wang, Study on subset size selection in digital image correlation for spackle patterns, Opt. Express 16 (2008) 7037–7048.

[37] Z. Wu, H. Rong, J. Zheng, W. Dong, An experimental investigation on the FPZ properties in concrete using digital image correlation technique, Eng. Fract. Mech. 78 (2011) 2978–2990.

[38] S.Y. Alam, A. Loukili, F. Grondin, Monitoring size effect on crack opening in concrete by Digital Image Correlation, Eur. J. Environ. Civ. Eng. 16 (2012) 1–19.

[39] Ł. Skarżyński, J. Kozicki, J. Tejchman, Application of DIC technique to concrete - study on objectivity of measured surface displacements, Exp. Mech. 53 (2013) 1545–1559.

[40] O. Orell, J. Vuorinen, J. Jokinen, H. Kettunen, P. Hytönen, J. Turunen, M. Kanerva, Characterization of elastic constants of anisotropic composites in compression using digital image correlation, Compos. Struct. 185 (2018) 176–185.

[41] Y. Su, Z. Gao, Q. Zhang, S. Wu, Spatial uncertainty of measurement errors in digital image correlation, Opt. Lasers Eng. 110 (2018) 113–121.

[42] L.I. Farfán-Cabrera, J.B. Pascual-Francisco, E.A. Gallardo-Hernández, O. Susarrey-Huerta, Application of digital image correlation technique to evaluate creep degradation of sealing elastomers due to exposure to fluids, Polym. Test. 65 (2018) 134–141.

[43] M. Mehdikhani, M. Aravand, B. Sabuncuoglu, M.G. Callens, S.V. Lomov, L. Gorbatikh, Full-field strain measurements at the micro-scale in fiber-reinforced composites using digital image correlation, Compos. Struct. 140 (2016) 192–201.

[44] M. Hamrat, B. Boulekbache, M. Chemrouk, S. Amziane, Flexural cracking behaviour of normal strength, high strength and high strength fiber concrete beams using Digital Image Correlation technique, Constr. Build. Mater. 106 (2016) 678–692.

[45] Y.-R. Zhao, L. Wang, Z.-K. Lei, X.-F. Han, Y.-M. Xing, Experimental study on dynamic mechanical properties of the basalt fiber reinforced concrete after the freeze thaw based on the digital image correlation method, Constr. Build. Mater. 147 (2017) 194–202.

[46] E. Pauwels, D. Van Loo, P. Cornillie, L. Brabant, L. Van Hoorebeke, An exploratory study of contrast agents for soft tissue visualization by means of high resolution X-ray computed tomography imaging, J. Microsc. 250 (2013) 21–31.

[47] T.K. Sampath, P. Simic, R. Sendak, N. Draca, A.E. Bowe, S. O'Brien, S.C. Schiavi, J. M. McPherson, S. Vukicevic, Thyroid-stimulating hormone restores bone volume, microarchitecture, and strength in aged ovariectomized rats, J. Bone Miner. Res. 22 (2007) 849–859.

[48] D. Cantre, E. Herremans, P. Verboven, J. Ampofo-Asiama, B.M. Nicolai, Characterization of the 3-D microstructure of mango (Mangifera indica L. cv. Carabao) during ripening using X-ray computed microtomography, Innovative Food Sci. Emerg. Technol. 24 (2014) 28–39.

[49] H.S. Tuan, W. Hutmacher, Application of micro-CT and computation modeling in bone tissue engineering, Comput. Aided Des. 37 (2005) 1151–1161.

[50] D. Tilman, F. Pfeiffer, O. Bunk, Ch. Grunzweig, E. Hempel, S. Popescu, P. Vock, Ch. David, Toward clinical X-ray phase-contrast CT: demonstration of enhanced soft-tissue contrast in human specimen, Invest. Radiol. 45 (2010) 445–452.

[51] K.I. Ignatiev, W.K. Lee, K. Fezzaa, S.R. Stock, Phase contrast stereometry: fatigue crack mapping in three dimensions, Philos. Mag. 85 (2005) 3273–3300.

[52] T.J. Marrow, J.Y. Buffiere, P.J. Withers, G. Johnson, D. Engelberg, High resolution X-ray tomography of short fatigue crack nucleation in austempered ductile cast iron, Int. J. Fatigue 26 (2004) 717–725.

[53] E.N. Landis, E.N. Nagy, D.T. Keane, Microtomographic measurements of internal damage in portland-cement-based composites, J. Aerosp. Eng. 10 (1997) 2–6.

[54] S. Lu, E.N. Landis, D.T. Keane, X-ray microtomographic studies of pore structure and permeability in Portland cement concrete, Mater. Struct. 39 (2006) 611–620.

[55] N. Burlion, D. Bernard, D. Chen, X-ray microtomography: aplication to microstructure analysis of a cementitious material during leaching process, Cem. Concr. Res. 36 (2006) 346–357.

[56] B. Chevalier, Introduction of X-ray CT application in geotechnical engineering - theory and practice, Conf. Ser. Mater. Sci. Eng. 10 (2010) https://doi.org/10.1088/1757-899X/10/1/012089.

[57] P. Besuell, G. Viggiani, N. Lenoir, J. Desrues, M. Bornert, X-ray micro-CT for studying strain localization in clay rocks under triaxial compression, in: Advances in X-ray Tomography for Geomaterials, 2nd International Workshop on X-Ray CT for Geomaterials, 2006, pp. 35–52.

[58] F. Prade, F. Schaff, S. Senck, P. Meyer, J. Mohr, J. Kastner, F. Pfeiffer, Nondestructive characterization of fiber orientation in short fiber reinforced polymer composites with X-ray vector radiography, NDT and E Int. 86 (2017) 65–72.

[59] R. Wang, X. Gao, J. Zhang, G. Han, Spatial distribution of steel fibers and air bubbles in UHPC cylinder determined by X-ray CT method, Constr. Build. Mater. 160 (2018) 39–47.

[60] T. Ponikiewski, J. Katzer, M. Bugdol, M. Rudzki, X-ray computed tomography harnessed to determine 3D spacing of steel fibers in self compacting (SCC) slabs, Constr. Build. Mater. 74 (2015) 102–208.

[61] G.L. Balázs, O. Czoboly, E. Lublóy, K. Kapitány, A. Barsi, Observation of steel fibres in concrete with Computed Tomography, Constr. Build. Mater. 140 (2017) 534–541.

[62] T. Ponikiewski, M. Gołaszewski, M. Rudzki, M. Bugdol, Determination of steel fibres distribution in self-compacting concrete beams using X-ray computed tomography, Arch. Civ. Eng. 2 (2015) 558–568 [xx] R. Wang, X. Gao, J. Zhang, G. Han, Spatial distribution of steel fibres and air bubbles in UHPC cylinder determined by X-ray CT method, Constr. Build. Mater. 160 (2018) 39–47..

[63] B. Zhou, Y. Uchida, Influence of flowablity, casting time and framework geometry on fiber orientation and mechanical properties of UHPFRC, Cem. Concr. Res. 95 (2017) 164–177.

[64] T. Ponikiewski, J. Katzer, M. Bugdol, M. Rudzki, Determination of 3D porosity in steel fibre reinforced SCC beams using X-ray computed tomography, Constr. Build. Mater. 68 (2014) 333–340.

[65] Y. Akkaya, A. Peled, S.P. Shah, Parameters related to fiber length and processing in cementitious composites, Mater. Struct. 33 (1999) 515–524.

[66] EN 12390-2:2009 Testing Hardened Concrete – Part 2: Making and Curing Specimens for Strength Tests.

[67] EN 12390-3:2009 Testing Hardened Concrete – Part 3: Compressive Strength of Test Specimens.

[68] V.C. Li, A simplified micromechanical model of compressive strength of fiber-reinforced cementitious composites, Cem. Concr. Res. 14 (2) (1992) 131–141.

[69] EN 12390-6:2011 Testing Hardened Concrete – Part 6: Tensile Splitting Strength of Test Specimens.

[70] A.M. Neville, Properties of Concrete, John Wiley & Sons, 1996.

[71] Instrukcja ITB 194/98 Badanie cech mechanicznych betonu na próbkach wykonanych w formach (in polish).

[72] A. Dehghan, K. Peterson, A. Shvarzman, Recycled glass fiber reinforced polymer additions to Portland cement concrete, Constr. Build. Mater. 146 (2017) 238–250.

[73] A. Noushini, K. Vessalas, G. Arabian, B. Samali, Drying shrinkage behaviour of fiber reinforced concrete incorporating polyvinyl alcohol fibers and fly ash, Adv. Civ. Eng. (2014). https://doi.org/10.1155.2014.836173.

[74] RILEM TC 162-TDF, Test and design methods for steel fiber reinforced concrete: bending test, Mater. Struct. 35 (2002) 579–582.

[75] EN 14651:2005+A1:2007 Test Method for Metallic Fiber Concrete. Measuring the Flexural Tensile Strength (limit of proportionality (LOP), residual).

[76] H.N. Linsbauer, E.K. Tschegg, Fracture energy determination of concrete with cube specimens, Zement und Beton 31 (1986) 38–40 (in german).

[77] S. Korte, V. Boel, W. De Corte, G. De Schutter, Static and fatigue fracture mechanics properties of self-compacting concrete using three-point bending tests and wedge splitting tests, Constr. Build. Mater. 57 (2014) 1–8.

[78] Y. Dai, D. Gruber, H. Harmuth, Determination of the behavior of MgO-refractories using multi-cycle wedge splitting test and digital image correlation, J. Eur. Ceram. Soc. 37 (15) (2017) 5035–5043.

[79] J. Suchorzewski, J. Tejchman, M. Nitka, Discrete element method simulations of fracture in concrete under uniaxial compression based on its internal structure, Int. J. Damage Mech. (2017), https://doi.org/10.1177/1056789517690915.

[80] Ł. Skarżyński, J. Tejchman, Modeling the effect of material composition on the tensile properties of concrete, in: Jaap Weerheijm (Ed.), Understanding the Tensile Properties of Concrete, vol. 48, Woodhead Publishing Limited, 2013, pp. 52–97.